Available online at www.sciencedirect.com
SCIENCE DIRECT®
Journal of Computational Physics 206 (2005) 661–683
JOURNAL OF COMPUTATIONAL PHYSICS
www.elsevier.com/locate/jcp

On the outflow boundary condition for external incompressible flows: A new approach

Nadeem Hasan [1], Syed Fahad Anwer [2], Sanjeev Sanghi *

Department of Applied Mechanics, Hauz Khas, Indian Institute of Technology – Delhi, New Delhi 110016, India

Received 7 April 2004; received in revised form 30 November 2004; accepted 5 December 2004
Available online 25 February 2005

Abstract

This work presents a new procedure for extrapolating velocities at the outflow boundary in the computations of incompressible flows around rigid bodies. The extrapolation procedure is based on the radial variation of the velocity field at large distances from the rigid body, which can be inferred from mass conservation and vorticity considerations. Since the extrapolation is based on these physical considerations, the proposed boundary condition is considered to be physically consistent. It has been demonstrated, via numerical simulations of 2D, laminar, incompressible, viscous flow past a circular and a square cylinder at $Re = 100$, that the application of the proposed boundary condition allows one to limit the unbounded domain to a small size (6–8 times the characteristic size of the body) without any significant change in the flow characteristics like the lift coefficient (C_L) and the Strouhal number (St). Thus, the proposed boundary conditions can enhance the computational efficiency of this class of flows.

Keywords: Outflow boundary condition; CFD; SMAC; Cylinder; Uniform flow; Strouhal number; Convective boundary condition; Low Reynolds number; Curvilinear coordinate system; Navier–Stokes equation

1. Introduction

In the CFD simulation of unsteady flow around a body in an open domain extending to infinity, the selection of proper outflow boundary conditions is a critical issue. In steady flows boundary conditions like pressure being constant or a vanishing gradient of any flow variable in the stream wise direction (Neumann

* Corresponding author. Tel.: +91 11 2659 1230.
E-mail addresses: nadarsh@lycos.com (N. Hasan), sfahadanw@yahoo.com (S.F. Anwer), sanghi@am.iitd.ernet.in (S. Sanghi).
[1] Tel.: +91 9810460347.
[2] Tel.: +91 9810444862.

0021-9991/$ - see front matter © 2005 Elsevier Inc. All rights reserved.
doi:10.1016/j.jcp.2004.12.025

boundary condition, NBC) are often used. The computations involving NBC, however, require the placement of the outflow boundary at a large distance in the downstream direction of the body. Okajima [1] and Stegall and Rockliff [2] employed NBC in computing 2D flows past a square cylinder. The outflow boundary in [1,2] was placed at 125 and 100 times the characteristic size of the cylinder, respectively. It is also known that for unsteady flows like the vortex shedding flows past bluff bodies, such conditions do not perform well and lead to distortion in the flow field near the outflow boundary.

One method which has been used by researchers, which seems to work well in unsteady flow situations for weakly convective flows, is the convective boundary condition (CBC), where an equation of type (1) is used on the outflow boundary

$$\frac{\partial \varphi}{\partial t} + \bar{u}\frac{\partial \varphi}{\partial n} = 0, \tag{1}$$

where φ is any flow variable like the velocity component and $\bar{u}$ is the convective velocity of flow structures, prescribed in a rather ad hoc way or by trial and error. Such a boundary condition was proposed by Orlanski [3] for the problems governed by hyperbolic system of equations.

The CBC has been used by Najjar and Vanka [4] and Najjar and Balachandran [5] in computing uniform flow past a normal flat plate. Cheng and Armfield [6] have employed it in computing uniform, two-dimensional flow past a circular cylinder. It has also been employed by Pauley et al. [7], Arnal et al. [8], Sohankar et al. [9] and Biswas and co-workers [10] for the computations of uniform, two-dimensional flow past a square cylinder. However, it is felt that the CBC lacks in a proper physical basis for elliptic and parabolic problems and it is also somewhat awkward to implement. The quantity $\bar{u}$ in (1) is loosely defined in the literature as different authors have defined it in a different manner [4–7]. The value of $\bar{u}$, which yields minimum distortion in the vorticity structure at the exit, has to be determined by trial.

A slightly different boundary condition has been used by Braza et al. [11]. To analyze the uniform flow past a circular cylinder, logarithmic-polar coordinates, defined as $x = \theta$ and $y = \ln r$, have been used. The outer boundary has been divided into a wake region and a region outside the wake. It is assumed that at infinity the flow is governed by Oseen's linearized equations which results in the following conditions at the outer boundary:

In the wake region:

$$\left(\frac{\partial \vec{V}}{\partial y}\right)_{y=y_\infty} \to 0. \tag{2}$$

Outside the wake region:

$$\vec{V}(x,y)_{y=y_\infty} \to \vec{U}_\infty, \tag{3}$$

where $\vec{U}_\infty$ is the free stream velocity.

The major drawback of this type of boundary condition is that a priori knowledge of the width of the wake on the outer boundary is needed for its application.

It is observed that the limitations of different types of boundary conditions employed by different workers are: (1) the numerical domain must extend to a large distance downstream of the body and (2) the application of the boundary condition involves guessing the value of some parameter (for e.g., $\bar{u}$ in CBC or width of the wake region [11]).

This work aims to circumvent these problems by providing an extrapolation procedure, which has a stronger physical basis and can be implemented in a straightforward manner without any trial or guess work. The primary motivation for this work comes from the fact that the computational efficiency of flows around immersed bodies can be enhanced if the size of the computational domain around the body can be

limited to relatively smaller dimensions without affecting the results significantly. This can be achieved if the boundary conditions employed at the outflow boundary are based on the physical behavior of the flow field at large distance from the body. Since the proposed boundary conditions involve physical considerations of mass conservation and vorticity, they have been referred to as the *physical boundary conditions* (PBCs).

The velocities at the outflow boundary are extrapolated from the interior in the computations of incompressible flows around rigid bodies, stationary or in motion, using structured or unstructured grids. The PBC involves an extrapolation procedure based on the expected radial variation of velocity field at large distances from the rigid body, which can be inferred from mass conservation and vorticity considerations. There is no ad hoc quantity needed to use this procedure. In case the grid lines are extending in a radial direction, then the application of the method is quite straightforward. Even if the grid lines are not radial, then also the method can be employed by suitable interpolation procedures. This has been demonstrated for a general curvilinear and a Cartesian grid. Extension to other grids (structured or unstructured) can be handled in a similar manner. Though the extrapolation procedure presented here is for 2D flows, the concept can be readily extended to three dimensions.

To demonstrate the validity of the procedure and to assess its performance, the problems of 2D, viscous, incompressible flow past a circular and a square cylinder are considered. Numerical simulations for both the cases have been carried out at $Re = 100$. This Re has been selected in order to demonstrate the performance of PBC in the unsteady, vortex shedding regime.

All numerical simulations have been carried out on a non-staggered, structured, curvilinear, body-fitted, O-type grid. The transformed Navier–Stokes equations have been discretized using the finite difference approach and a semi-explicit pressure correction algorithm is employed [12]. Numerical simulations, for circular as well as the square cylinder, have been carried out by placing the far field boundary at different distances from the body. The maximum and minimum distances considered are 20 and 6 times the characteristic size of the body, respectively. Thus, the extent to which the numerical domain can be shrunk when the PBC is applied can be estimated. Further, the effect of limiting the domain to progressively smaller dimensions can also be quantitatively assessed. For different boundary placements, the lift coefficient (C_L), the drag coefficient (C_D), Strouhal number (St), vorticity and velocity fields near the exit and near the cylinder are compared.

2. Mathematical formulation

In this section, the variation of the velocity field in the radial direction at very large distances from the body is deduced. The procedure to exploit this radial behavior in extrapolating the velocities from the interior to the outflow portion of the artificial boundary for radial grids, structured body fitted grids and structured Cartesian grids is also presented.

2.1. Boundary conditions at infinity

The behavior of 2D velocity field at large distances from a rigid infinite body placed in a uniform stream of velocity $\vec{U}_\infty$ is analyzed. Consider a surface S of unit depth enclosing the body as shown in Fig. 1. Let $\vec{V}(\vec{r},t)$ represent the velocity field around the body. From the analytical point of view, it is known that

$$\lim_{|\vec{r}|\to\infty} \vec{V}(\vec{r},t) = \vec{U}_\infty. \tag{4}$$

In a numerical simulation it is impractical to use (4) as it involves the placement of the outer boundary at very large distances from the body. If the analytical behavior of $\vec{V}(\vec{r},t)$ is known as $|\vec{r}|\to\infty$, then it can be effectively utilized to numerically incorporate the analytical behavior in the computer simulations. The

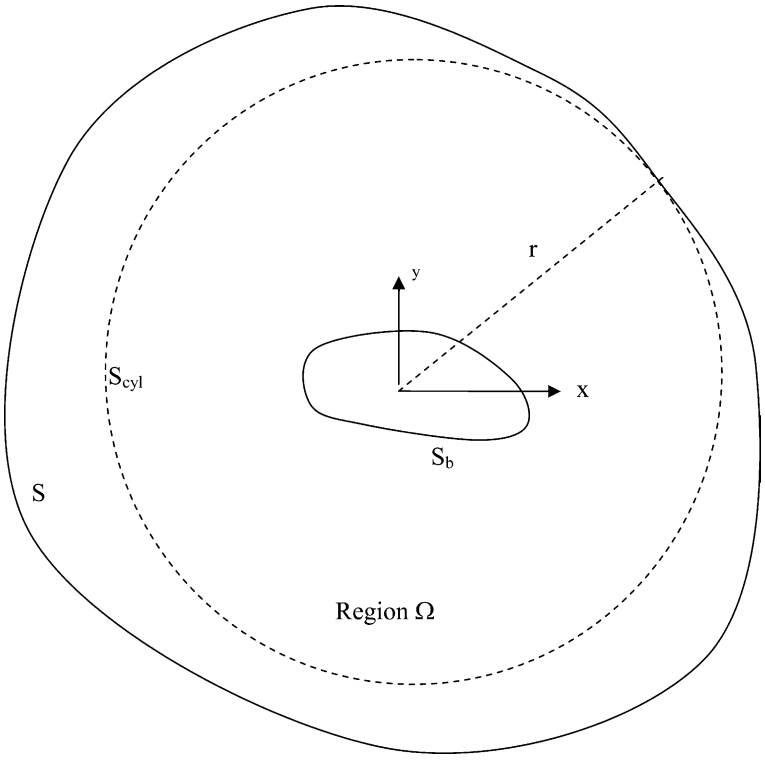

Fig. 1. Illustration for any external surface S enclosing a rigid body S_b and region Ω.

following considerations provide the desired behavior. Let the perturbed velocity field $\vec{V}'(\vec{r},t)$ generated due to the presence of the body be defined as

$$\vec{V}'(\vec{r},t) = \vec{V}(\vec{r},t) - \vec{U}_\infty. \tag{5}$$

From continuity equation it can be deduced that

$$\vec{\nabla}\cdot\vec{V}' = \vec{\nabla}\cdot\vec{V} = 0. \tag{6}$$

Applying Gauss theorem to the perturbed velocity field,

$$\int_\Omega \left(\vec{\nabla}\cdot\vec{V}'\right) \mathrm{d}\forall = \int_S \vec{V}'\cdot\hat{n}\,\mathrm{d}S - \int_{S_b}\vec{V}'\cdot\hat{n}\,\mathrm{d}S = 0 \Rightarrow \int_S \vec{V}'\cdot\hat{n}\,\mathrm{d}S = \int_{S_b}\vec{V}'\cdot\hat{n}\,\mathrm{d}S. \tag{7}$$

The perturbed velocity field at the surface of the body is given as

$$\vec{V}' = \vec{U}_b(\vec{r},t) - \vec{U}_\infty, \tag{8}$$

where $\vec{U}_b(\vec{r},t)$ is the velocity at the surface of the body (assuming the body to be deformable). Substituting (8) in (7) leads to

$$\int_S \vec{V}'\cdot\hat{n}\,\mathrm{d}S = \int_{S_b}\left(\vec{U}_b(\vec{r},t) - \vec{U}_\infty\right)\cdot\hat{n}\,\mathrm{d}S. \tag{9}$$

Since $\int_{S_b}\vec{U}_\infty\cdot\hat{n}\,\mathrm{d}S = \vec{U}_\infty\cdot\int_{S_b}\hat{n}\,\mathrm{d}S = 0$, it can be deduced that

$$\int_S \vec{V}' \cdot \hat{n}\, \mathrm{d}S = \int_{S_b} \vec{U}_b(\vec{r}, t).\hat{n}\, \mathrm{d}S. \tag{10}$$

The integral on the right-hand side in (10) represents the rate of change of the volume of the body and it vanishes for a non-deforming rigid body.

Thus,

$$\int_S \vec{V}' \cdot \hat{n}\, \mathrm{d}S = 0. \tag{11}$$

The integral in (11) must be independent of the shape of the surface S and its distance from the body. Hence, to analyze the local behavior of the velocity field at any point on the surface S, consider a local cylindrical surface S_{cyl} of radius 'r' and unit depth passing through the point under consideration (Fig. 1)

$$\oint_{S_{cyl}} (v_r - V_{r\infty}) r\, \mathrm{d}\theta = 0. \tag{12}$$

Hence it can be inferred that if the integral must vanish for infinitely large 'r', then $(v_r - V_{r\infty})$ must behave at least as follows:

$$(v_r - V_{r\infty}) \sim \frac{1}{r^2}, \quad r \to \infty, \text{ where } r = |\vec{r}|. \tag{13}$$

It can be readily verified that as $r \to \infty$, $v_r \to V_{r\infty}$, where $V_{r\infty}$ is the radial component of the undisturbed uniform velocity field $\vec{U}_\infty$. These conditions have been described in [13] but have not been used, to the best of the knowledge of the authors, in the numerical computations. The expression in (13) actually implies that if the perturbed radial velocity is expanded in a power series of $(1/r)$ as r approaches infinity, the expansion must begin with a quadratic term.

To obtain the behavior of the complete 2D velocity field, one needs to analyze the behavior of v_θ as well. For this purpose consider two irreducible circuits C_1 and C_2 enclosing the body as shown in Fig. 2. Let D denote the region between C_1 and C_2. Taking the curl of (5),

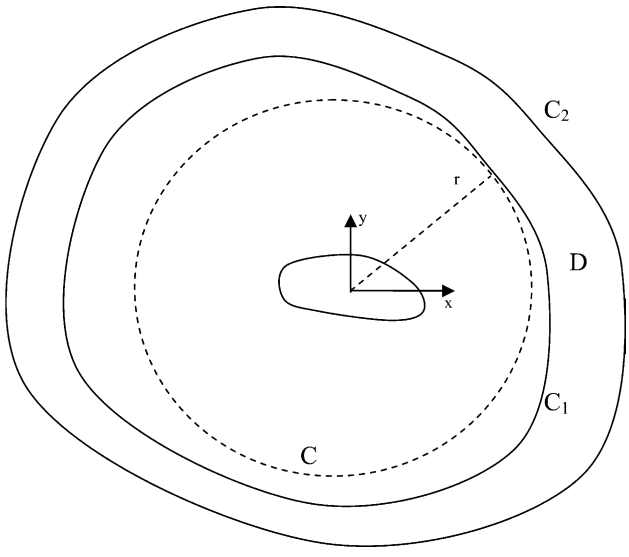

Fig. 2. Illustration of two irreducible circuits C_1 and C_2 enclosing a region D.

$$\vec{\varpi}' = \vec{\varpi}. \tag{14}$$

Eq. (14) is the mathematical statement of the fact that the presence of the body in a uniform stream generates the vorticity in the flow field. If Γ_1 and Γ_2 are the counterclockwise circulations around C_1 and C_2, respectively, then utilizing Stokes theorem leads to

$$\int_D \varpi' \, \mathrm{d}A = \Gamma_1 - \Gamma_2. \tag{15}$$

In viscous flows, far away from the body, the vorticity is usually quite small. If C_1 and C_2 are everywhere far from the body, then the left-hand side of (14) is generally quite small and negligible. Since C_1 and C_2 are two arbitrary contours, the circulation Γ around a circuit becomes nearly constant and approximately independent of the shape and distance of the circuit from the body. To analyze the radial behavior of v_θ at a point on the contour C_1, consider a circular contour C of radius 'r' passing through the point under consideration on C_1 at a large distance from the body (Fig. 2). The circulation on C is given as:

$$\Gamma = \oint_C (v_\theta - V_{\theta\infty}) r \, \mathrm{d}\theta. \tag{16}$$

Since Γ is approximately constant and independent of 'r' then there are only two possibilities, either Γ is non-zero or zero

$$\oint (v_\theta - V_{\theta\infty}) r \, \mathrm{d}\theta = 0 \quad \text{if } \Gamma = 0,$$

$$\oint (v_\theta - V_{\theta\infty}) r \, \mathrm{d}\theta \neq 0 \quad \text{if } \Gamma \neq 0.$$

Thus, as $r \to \infty$, $(v_\theta - V_{\theta\infty})$ must behave as follows:

$$(v_\theta - V_{\theta\infty}) \sim \frac{1}{r^2} \quad \text{if } \Gamma = 0, \tag{17a}$$

$$(v_\theta - V_{\theta\infty}) \sim \frac{1}{r} \quad \text{if } \Gamma \neq 0. \tag{17b}$$

Again it is observed that as $r \to \infty$, $v_\theta \to V_{\theta\infty}$, where $V_{\theta\infty}$ is azimuthal component of undisturbed velocity field at infinity. The circulation Γ for C_1 can be computed in a direct non-iterative manner at the given time since the velocity field is being calculated in the interior. As with the perturbed radial velocity, relations (17a) and (17b) are truncated forms of the more general asymptotic expansions involving higher powers of $(1/r)$.

2.2. Implementation of the boundary condition

The behavior of the velocity field as given by (13) and (17) at large distances from the body can be utilized in a straightforward manner to extrapolate velocities from the interior on to the outflow boundary of the computational domain. However, since (13) and (17) express the variation of velocity field in the radial direction, it is quite obvious that the extrapolation must take place in the radial direction. This is not so restrictive as it appears. By employing suitable interpolation procedures for non-radial grids, the radial extrapolation of velocities onto the outflow boundary can be achieved in a straightforward manner. The implementation aspects of the boundary conditions given by (13) and (17) on structured polar, structured body fitted and Cartesian grids are discussed below.

2.2.1. Structured polar grid

The extrapolation procedure is straightforward to apply on a structured polar grid and is explained with the aid of Fig. 3(a). Fig. 3(a) shows a portion of two constant radii curves $r = r_1$ and $r = r_2$ and a constant θ line in a structured polar grid. The outer boundary of the domain in the physical plane is represented by $r = r_2$ and $r = r_1$ is the constant radius curve adjacent to $r = r_2$. The extrapolation

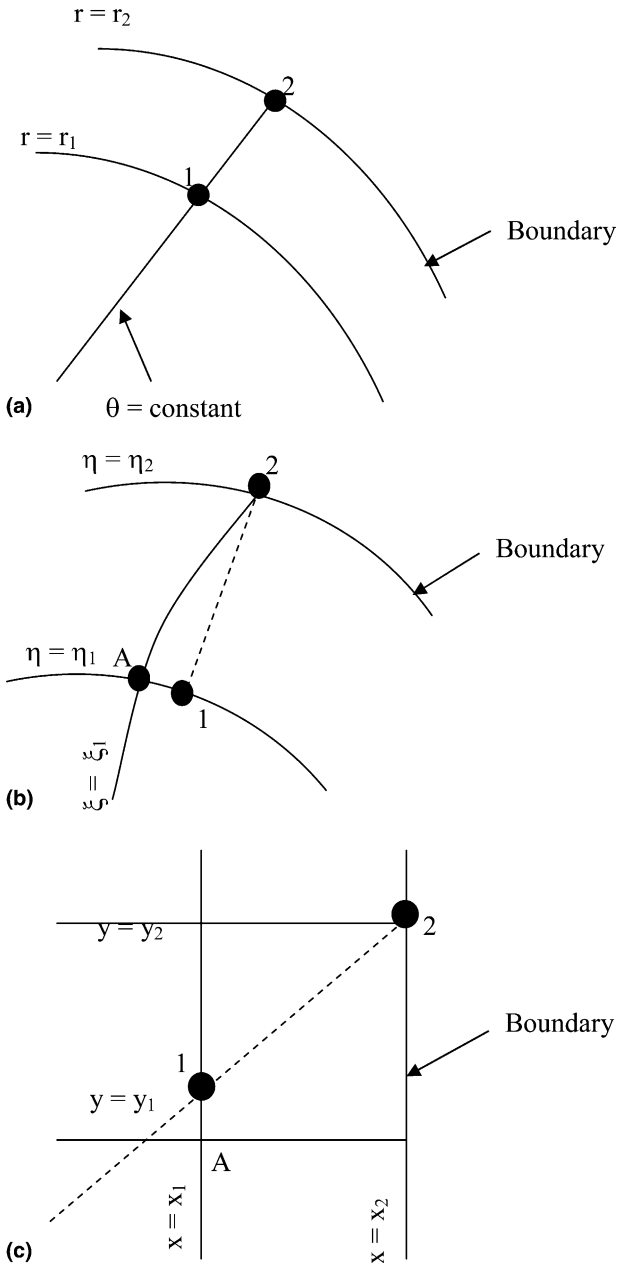

Fig. 3. Illustrations for implementation of boundary conditions on (a) radial grid, (b) body fitted grid, (c) Cartesian grid.

involves obtaining the velocity field at a typical boundary grid point 2 on r_2. The grid point 1 lies on $r = r_1$ and also on the constant θ line connecting point 2 to point 1. Since point 1 is the nearest radial neighbor of point 2 in the structured grid, the velocity components v_r and v_θ at point 2 can be readily computed using (13) and (17) as:

$$(v_r - V_{r\infty})_1 r_1^2 = (v_r - V_{r\infty})_2 r_2^2.$$

Since the extrapolation is radial, $(V_{r\infty})_1 = (V_{r\infty})_2$

$$(v_r)_2 = \left\{\frac{r_1}{r_2}\right\}^2 (v_r)_1 + (V_{r\infty})_2 \left\{1 - \left(\frac{r_1}{r_2}\right)^2\right\}. \tag{18}$$

Similarly,

$$\begin{aligned} (v_\theta)_2 &= \left\{\frac{r_1}{r_2}\right\}^2 (v_\theta)_1 + (V_{\theta\infty})_2 \left\{1 - \left(\frac{r_1}{r_2}\right)^2\right\} \quad \text{if } \Gamma_{r=r_1} = 0, \\ (v_\theta)_2 &= \left\{\frac{r_1}{r_2}\right\} (v_\theta)_1 + (V_{\theta\infty})_2 \left\{1 - \left(\frac{r_1}{r_2}\right)\right\} \quad \text{if } \Gamma_{r=r_1} \neq 0. \end{aligned} \tag{19}$$

For grids which do not possess radial grid lines, Eqs. (18) and (19) can still be utilized, provided that: (1) the nearest radial neighbor of the boundary point under consideration can found in the grid and (2) a suitable interpolation procedure is devised to obtain the values of the radial and circumferential velocities at this point. This is shown specifically for a structured body fitted and a Cartesian grid in the succeeding subsections.

2.2.2. Structured body fitted grid

Fig. 3(b) shows a portion of two constant η lines $\eta = \eta_1$ and $\eta = \eta_2$ and a constant ξ line $\xi = \xi_1$. The outer boundary of the domain in the physical plane is represented by $\eta = \eta_2$ and $\eta = \eta_1$ is the constant η curve adjacent to $\eta = \eta_2$. The extrapolation involves obtaining the velocity field at a typical boundary grid point 2 on η_2. The grid point A is the intersection point of $\eta = \eta_1$ and $\xi = \xi_1$ curves. Since $\xi = \xi_1$ line in general may not be radial, the radial line from point 2 intersects $\eta = \eta_1$ curve at some point 1 in the neighborhood of point A (Fig. 3(b)). Thus, point 1 is the nearest radial neighbor of point 2 on the structured grid. To locate point 1, it is sufficient to determine the value of the ξ coordinate associated with the point. This can be done by the following procedure. Let the coordinates of point 1 and 2 be given as (x_1, y_1) and (x_2, y_2), respectively. The coordinates of point 2 are known from the grid. The coordinates of point 1 can be related to the coordinates of the neighboring point A by expanding the coordinates in a Taylor series around the point A. This yields

$$y_1 = y_A + \left(\frac{\partial y}{\partial \xi}\right)_A (\xi_1 - \xi_A) + O\left[(\xi_1 - \xi_A)^2\right], \tag{20}$$

$$x_1 = x_A + \left(\frac{\partial x}{\partial \xi}\right)_A (\xi_1 - \xi_A) + O\left[(\xi_1 - \xi_A)^2\right]. \tag{21}$$

Since the points 1 and 2 lie on the same radial line,

$$\frac{y_1}{x_1} = \frac{y_2}{x_2}. \tag{22}$$

Combining (20)–(22), a first order accurate expression for $(\xi_1 - \xi_A)$ can be written as

$$(\xi_1 - \xi_A) = \frac{(y_2 x_A - y_A x_2)}{\left(\left\{\frac{\partial y}{\partial \xi}\right\}_A x_2 - \left\{\frac{\partial x}{\partial \xi}\right\}_A y_2\right)}. \tag{23}$$

The radial and circumferential velocities at point 1 can now be readily determined again through a Taylor expansion for any flow variable in the neighborhood of point A as given below:

$$\phi_1 = \phi_A + \left(\frac{\partial \phi}{\partial \xi}\right)_A (\xi_1 - \xi_A) + \left(\frac{\partial^2 \phi}{\partial \xi^2}\right)_A \frac{(\xi_1 - \xi_A)^2}{2} + O[(\xi_1 - \xi_A)^3]. \tag{24}$$

Hence, the radial and circumferential velocities are first obtained at point A and the subsequent application of (24) yields the corresponding velocities at point 1. Once the radial and circumferential velocities at point 1 are known, Eqs. (18) and (19) can be readily utilized to yield the corresponding velocities at the boundary point 2. It is worth mentioning here that computations using body fitted coordinates generally involve Cartesian velocity components. Thus, vector transformation laws have to be used to convert Cartesian velocity components into polar ones and vice versa as per the requirements.

From the numerical point of view, usage of (18) and (19) requires computation of $(v_r)_1$, $(v_\theta)_1$ and Γ on $\eta = \eta_1$. Since the velocity field is being computed in the interior with the help of basic equations of flow, it is known at the time of application of boundary condition. So these quantities can be readily computed in a direct non-iterative manner adding little to the overall computational efforts.

2.2.3. Cartesian grid

Fig. 3(c) illustrates the procedure for implementation of boundary conditions on a Cartesian structured grid. Let $x = x_2$ be the outflow boundary grid line and $x = x_1$ be the adjacent grid line. Let ϕ be the slope of the radial line drawn from a typical boundary grid point 2. This radial line intersects $x = x_1$ at y_1 which can be written as

$$y_1 = y_2 - (x_2 - x_1)\tan\phi. \tag{25}$$

This gives the location of point 1 on grid line $x = x_1$. Let the nearest neighbor of point 1 on the grid line $x = x_1$ be point A (Fig. 3(c)). The value of any flow variable can be obtained at point 1 employing Taylor expansion around point A

$$\phi_1 = \phi_A + \left(\frac{\partial \phi}{\partial y}\right)_A (y_1 - y_A) + \left(\frac{\partial^2 \phi}{\partial y^2}\right)_A \frac{(y_1 - y_A)^2}{2} + O[(y_1 - y_A)^3]. \tag{26}$$

Both $(v_r)_1$ and $(v_\theta)_1$ can thus be obtained at point 1 from (26). Finally, the boundary values of v_r and v_θ at point 2 are obtained from (18) and (19).

3. Governing equations and numerical scheme

In this section, the governing equations in generalized body fitted coordinates are presented. The flow past a circular and a square cylinder has been computed using a body fitted coordinate system. For this purpose an elliptic grid with an o-type of topology is generated around the body [14]. Figs. 4(a) and (b) show the typical domains of the numerical calculations in the physical plane together with the boundary fitted coordinate system for the circular and the square cylinder, respectively. The approaching free stream is aligned with the positive x-direction for both the problems. The simulations are carried out using a semi-explicit, pressure correction algorithm [12] similar to SMAC. A brief description of the numerical scheme is given in Section 3.2.

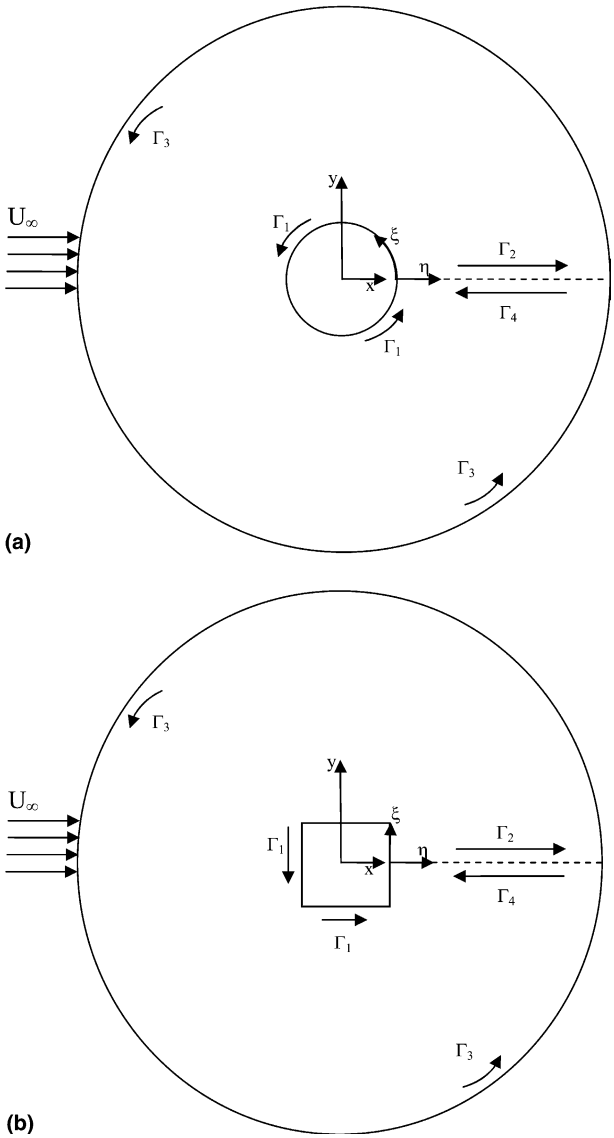

Fig. 4. Illustrations showing definitions of Cartesian and body fitted coordinates employed for (a) circular cylinder (b) square cylinder.

3.1. Governing equations

The non-dimensional governing equations (continuity and momentum), transformed in the body fitted coordinate system [14], are given as follows:

Continuity:

$$\left(\frac{y_\eta}{J}\frac{\partial}{\partial\xi}-\frac{y_\xi}{J}\frac{\partial}{\partial\eta}\right)U+\left(-\frac{x_\eta}{J}\frac{\partial}{\partial\xi}+\frac{x_\xi}{J}\frac{\partial}{\partial\eta}\right)V=0. \tag{27}$$

x-Momentum:

$$\frac{\partial U}{\partial \tau}+U^{\xi}\frac{\partial U}{\partial \xi}+U^{\eta}\frac{\partial U}{\partial \eta}=-\left(\frac{y_{\eta}}{J}\frac{\partial p}{\partial \xi}-\frac{y_{\xi}}{J}\frac{\partial p}{\partial \eta}\right)+\left(\frac{1}{Re}\right)\left(\alpha\frac{\partial^2 U}{\partial \xi^2}-2\beta\frac{\partial^2 U}{\partial \xi\,\partial \eta}+\gamma\frac{\partial^2 U}{\partial \eta^2}\right). \tag{28}$$

y-Momentum:

$$\frac{\partial V}{\partial \tau}+U^{\xi}\frac{\partial V}{\partial \xi}+U^{\eta}\frac{\partial V}{\partial \eta}=-\left(-\frac{x_{\eta}}{J}\frac{\partial p}{\partial \xi}+\frac{x_{\xi}}{J}\frac{\partial p}{\partial \eta}\right)+\left(\frac{1}{Re}\right)\left(\alpha\frac{\partial^2 V}{\partial \xi^2}-2\beta\frac{\partial^2 V}{\partial \xi\,\partial \eta}+\gamma\frac{\partial^2 V}{\partial \eta^2}\right). \tag{29}$$

U^{ξ} and U^{η} are the dimensionless velocities in ξ and η directions.

$$\begin{aligned} U^{\xi}&=\left(\frac{y_{\eta}}{J}\right)U-\left(\frac{x_{\eta}}{J}\right)V,\\ U^{\eta}&=-\left(\frac{y_{\xi}}{J}\right)U+\left(\frac{x_{\xi}}{J}\right)V. \end{aligned} \tag{30}$$

In (28) and (29) p is the dimensionless pressure defined as

$$p=\frac{P-P_{\infty}}{\rho U_{\infty}^2}, \tag{31}$$

where P and P_{∞} are the dimensional pressure and the undisturbed free stream pressure, respectively.

The quantities α, β, γ and J appearing in Eqs. (27)–(29) are defined as

$$\begin{aligned} \alpha&=(y_{\eta}^2+x_{\eta}^2)/J^2,\\ \beta&=(y_{\eta}y_{\xi}+x_{\eta}x_{\xi})/J^2,\\ \gamma&=(y_{\xi}^2+x_{\xi}^2)/J^2,\\ J&=x_{\xi}y_{\eta}-x_{\eta}y_{\xi}. \end{aligned} \tag{32}$$

The various global parameters characterizing the flow are defined as

$$\text{Lift coefficient}=C_{\mathrm{L}}=\frac{2F_y}{\rho U_{\infty}^2\ell}, \tag{33a}$$

$$\text{Drag coefficient}=C_{\mathrm{D}}=\frac{2F_x}{\rho U_{\infty}^2\ell}, \tag{33b}$$

and

$$\text{Strouhal number}=St=\frac{f\ell}{U_{\infty}}, \tag{33c}$$

where F_x and F_y are the sum of both viscous and pressure forces in the x and y directions, respectively, f is the shedding frequency, U_{∞} is the magnitude of the undisturbed free stream velocity and ℓ is the characteristic length scale. The characteristic length scales for the circular and square cylinder are taken to be the diameter D and the length of the edge H, respectively.

3.2. Numerical scheme

To capture the unsteady physics of the flow, a semi-explicit, pressure correction type of scheme is employed on a non-staggered curvilinear mesh. The concept of momentum interpolation of Rhie and Chow [15] is utilized in order to avoid grid scale pressure oscillations that can result due to the decoupling between the velocity and the pressure at a grid point. The scheme is described by Hirsch [12] and is conceptually

similar to the SMAC algorithm given by Amsden and Harlow [16]. Kim and Benson [17] and Cheng and Armfield [6] have demonstrated the computational efficiency of SMAC scheme over the SIMPLE, SIMPLEC and PISO methods for computing of unsteady, incompressible flows. Thus, the present work also utilizes a scheme that is essentially similar to SMAC.

The scheme involves an explicit, first order time integration of the momentum equations to obtain a guessed velocity field at the new time level. The guessed velocity field does not satisfy the continuity equation at the new time level. It is then corrected via a pressure correction field in a manner so as to preserve the vorticity while bringing the divergence of velocities near to zero. The pressure correction field is obtained via the pressure correction Poisson equation (PCPE). This procedure is similar to the SMAC algorithm [16].

The discretization of PCPE needs to be handled carefully as the central discretization of terms on both sides of the equation leads to an effective discrete equation on a mesh twice as coarse as the actual grid. Further, the central discretization of the divergence term involving guessed velocities results in the decoupling of pressure and velocity. These effects generally lead to spurious grid scale pressure oscillations [6,18]. To ensure that the scheme does not permit such non-physical solutions specifically due to the above-mentioned reasons, the discretization of PCPE has to be done with care. The Laplace operator in PCPE is discretized in a compact manner by defining the discrete divergence operator on points midway between the grid points. The divergence of guessed velocity is obtained through the momentum interpolation procedure [15]. The momentum interpolation involves obtaining the velocities midway between adjacent nodes through a special procedure which helps in maintaining the coupling between the velocity and pressure.

In the discretization of momentum equations, the convection terms are discretized using fourth order central differencing scheme in the interior and second order central differencing near the cylinder and near the outer boundary. The viscous terms are discretized using fourth order central differencing scheme. The pressure gradients are discretized using second order central differencing. The discrete Poisson equation is solved using a nine point SIP procedure [18] with a residual tolerance of 10^{-3}.

3.3. Boundary and initial conditions

In the numerical scheme employed, boundary conditions have to be specified for velocities, pressure correction field and the pressure field. The velocity field is specified as uniform flow at the inflow portion of the outer boundary. On the outflow portion, it is extrapolated from the interior using (18) and (19). The no-slip condition is specified on the solid surface. At the solid surface and at the inflow boundary, the gradient of pressure correction field in the η direction is taken to be zero. At the outflow, the pressure correction is taken to be zero. The conditions on pressure correction are essentially the same as employed in [6]. The boundary conditions on pressure are to be selected much more carefully if the numerical simulations are to be carried out on a heavily truncated domain. The pressure on the solid surface and on the inflow boundary is updated by obtaining the value of pressure gradient in the η direction through full momentum equations as follows:

$$\frac{\partial p}{\partial \eta} = \left(\frac{\partial p}{\partial x}\right)\left(\frac{\partial x}{\partial \eta}\right) + \left(\frac{\partial p}{\partial y}\right)\left(\frac{\partial y}{\partial \eta}\right). \tag{34}$$

The pressure gradients in the x and y directions at the boundaries (solid and inflow) are obtained through the x and y momentum equations, respectively. At the outflow, the traction free conditions proposed by Gresho [19] are employed to obtain the pressure. This leads to a condition of the following type:

$$-P + 2\mu\left(\frac{\partial u_n}{\partial n}\right) = 0. \tag{35}$$

In the above equation 'n' is the local normal direction at the boundary. This condition has also been used by Cheng and Armfield [6]. Initially, the flow field is taken to be uniform having undisturbed free stream values of velocity and pressure in the interior of the flow domain.

4. Validation

Validation of the code is done by solving uniform flow past a circular cylinder for a range of Re from 20 to 100. The values of Re are based on the cylinder diameter. This range of Re spans both the steady and the unsteady regimes. Validation is done both quantitatively and qualitatively on a grid of 91×121 with the outer boundary placed at 20 diameters away. In the steady flow regime, the length of separation and the pressure distribution over the cylinder are compared. Table 1 compares the dimensionless length of the separation zone in the wake (L/D) at $Re = 20$ and $Re = 40$ to the numerical results in [6,11]. It can be seen that the deviation is less than 1%. In Fig. 5, temporal growth of the separation length at $Re = 40$ is compared with the experimental data of Coutanceau and Bouard [20] and with the numerical results in [6]. It can be seen that the results from the present work match very well with those given in [6,20].

The other important characteristic is the pressure distribution over the cylinder. The coefficient of pressure (C_p) at $Re = 40$ is plotted over the upper half of cylinder in Fig. 6. It is defined as:

$$C_p = 1 + \frac{P - P_0}{\rho U_\infty^2}. \tag{36}$$

In (36) P_0 is the dimensional pressure at the front stagnation point. It can be seen that the present calculations agree well with the experimental data of Grove et al. [21] and the numerical data in [6].

In the unsteady vortex shedding regime, an important flow characteristic is the Strouhal number (St) as defined in (33c). In this unsteady regime Re was varied from 50 to 100 in steps of 10. Fig. 7 compares the variation of St with Re for the present calculations with the results given by Barkley and Henderson [22]. It is observed that the deviation between the two data is less than 1%.

Simulations were carried out for $Re = 46$ and $Re = 47$ to check if the numerical scheme is able to predict the inception of instability. Barkley and Henderson [22] predicted that the breakdown of steady state takes place at $Re = 46 \pm 1$ through a supercritical Hopf bifurcation. It is observed that the flow remains steady at $Re = 46$. At $Re = 47$ a single frequency periodic flow with vortex shedding is observed (Fig. 8).

5. Results and discussion

A suitable outflow boundary condition for flows around immersed bodies should possess two important properties: It should allow the flow to exit the domain with minimum distortion of the flow structure, and it should permit the computations on a heavily truncated domain with negligible effect on the flow as the artificial boundary is brought closer to the body. For problems involving an artificial boundary, introduced to truncate an otherwise infinite domain, it is of interest to examine the extent of truncation upto which a

Table 1
Length of separation zone in the wake at different Reynolds number

Reynolds number (Re)	Length of separation zone in the wake (L/D)		Error %
	PBC	Published	
20	0.9328	0.94 [6]	0.7%
40	2.3068	2.30 [6,11]	0.2%

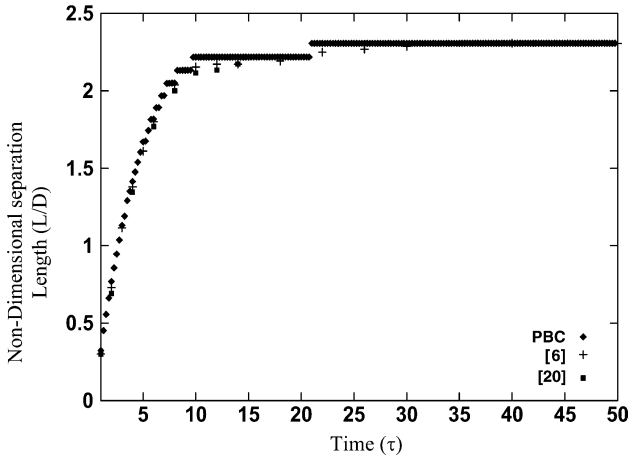

Fig. 5. Variation of dimensionless separation length (L/D) with time for circular cylinder at $Re = 40$.

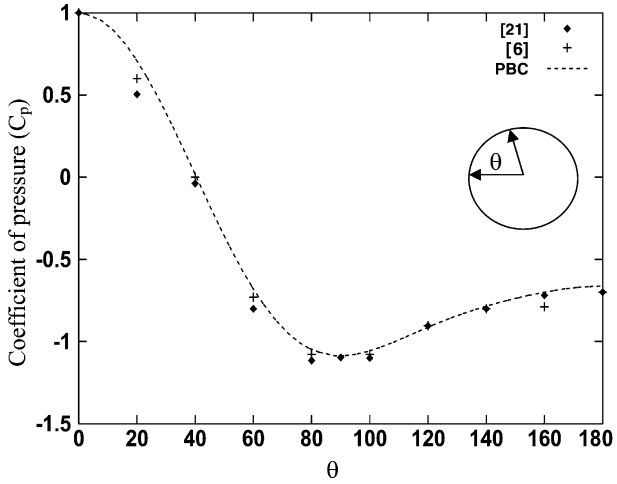

Fig. 6. Variation of coefficient of pressure over the upper surface for circular cylinder at $Re = 40$.

given outflow boundary condition retains these two properties. This has a direct bearing on the cost of computing such flows. In this section, the performance of PBC is examined in the context of the above-mentioned criteria.

To assess the performance of PBC, computations were carried out for uniform flow past a circular cylinder and a square cylinder at $Re = 100$. At this Re, the flow for both configurations is unsteady and involves vortex shedding. The effect of shortening the outer boundary is studied by placing the outer boundary at distances of 6, 8, 10, 12 and 20ℓ, where 'ℓ' is the characteristic size of the body. These distances are measured from the center of the cylinders. To ensure that the computations carried out for different levels of truncation of the flow domain reflect the effects of boundary placement only, the grid generated for the case of 20ℓ is simply truncated and employed for the other cases. This ensures that the grid spacings remain the same for all the cases. To assess the effect of boundary placement on the flow structure of the wake, particularly, near the outflow boundary, the vorticity and streamline contours are plotted. To

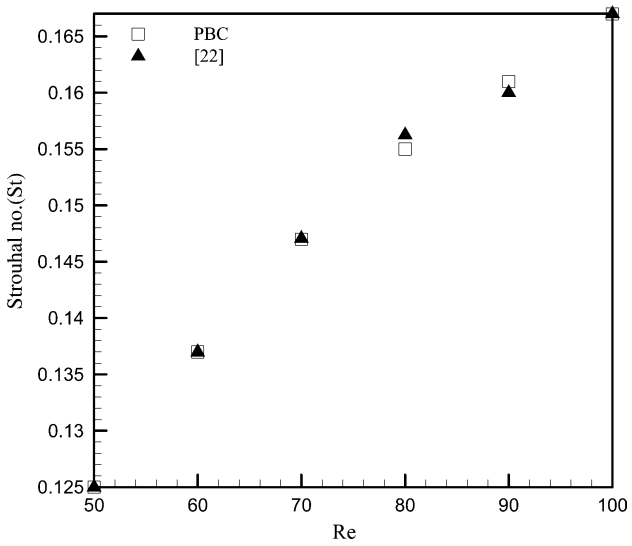

Fig. 7. Variation of Strouhal number with *Re*.

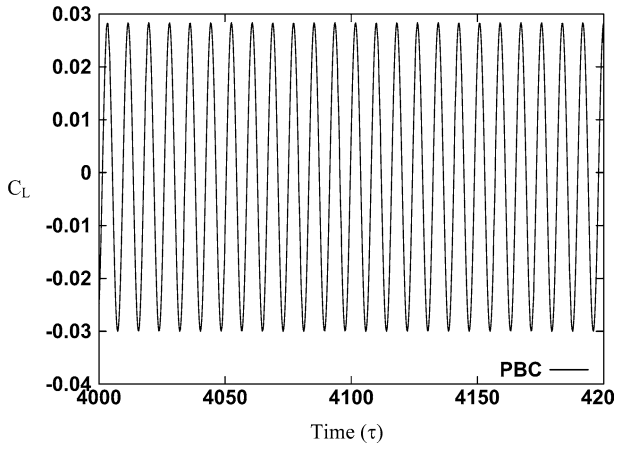

Fig. 8. Variation of C_L with time at $Re = 47$.

examine the effect of boundary placement on the flow field near the cylinders, parameters like Strouhal number (St), peak values of lift coefficient (C_L) and time average drag coefficient ($\bar{C}_D$) are compared. The time histories of C_L are also compared.

The grids employed for cases of 6, 8, 10, 12, 20ℓ have 121×124, 121×138, 121×148, 121×157 and 121×181 points, respectively. The grids are stretched in the physical space in the η direction. A non-dimensional time step of 1×10^{-3} has been employed for all the cases.

5.1. Uniform flow past a circular cylinder ($Re = 100$)

Table 2 shows the effect of placement of outflow boundary at 6D, 8D, 10D, 12D and 20D for the case of circular cylinder at $Re = 100$ (where 'D' is the diameter of the cylinder). The parameters like St and peak

Table 2
The effect of far field boundary placement on Strouhal number and peak lift coefficient for uniform flow past the circular cylinder at $Re = 100$

Far field boundary	Strouhal number (St)	Peak lift coefficient (C_L)	Average drag coefficient ($\bar{C}_D$)
6D	0.1667	0.319	1.4239
8D	0.1667	0.307	1.3812
10D	0.1667	0.298	1.3581
12D	0.1667	0.305	1.3606
20D	0.1667	0.2958	1.3606
Numerical [11,22,23]	0.16	0.295	1.36
Experimental [20]	0.1667	–	–

values of C_L are compared with the experimental and numerical values in [11,20]. It can be seen that as the outflow boundary is brought nearer to the cylinder from a distance of 20D to 6D, the deviations in the peak values of C_L from the value reported in [11] increase from 0.2% to 5%. However, there is no deviation in St and the values at different boundary placements matches with those in [11,20]. The values of $\bar{C}_D$ match very well for the case of 20D with the data from [23]. The increase in $\bar{C}_D$ as the boundary is brought closer from a distance of 20D to 6D is about 4.4%.

Fig. 9 compares the time evolution of C_L for cases of 20D, 12D and 8D. It is interesting to observe that the growth rate and the frequency of the perturbations are not affected significantly. Only a phase shift is observed as the outer boundary is brought closer. This result is quite significant as it demonstrates that the usage of PBC on a heavily truncated domain does not significantly affect the amplitude growth rate and the oscillation frequency of the unstable mode or perturbation. The increase in the deviation observed in the peak values of C_L, as the outer boundary is brought closer to the body, is inevitable as the outflow boundary conditions have been derived from the anticipated behavior of the flow field at large distances.

Figs. 10(a)–(e) show the instantaneous vorticity contours in the wake region and near the exit for outer boundary placements at 6D, 8D, 10D, 12D and 20D, respectively. Since there is a phase shift, the snaps are

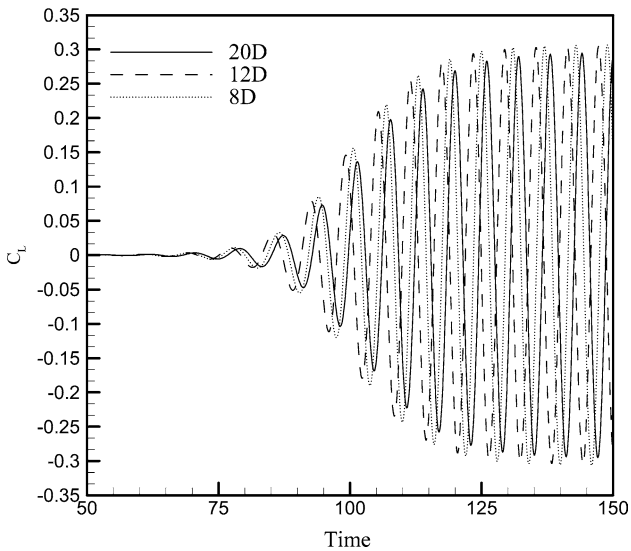

Fig. 9. Variation of C_L at $Re = 100$ for different boundary placements for flow past a circular cylinder.

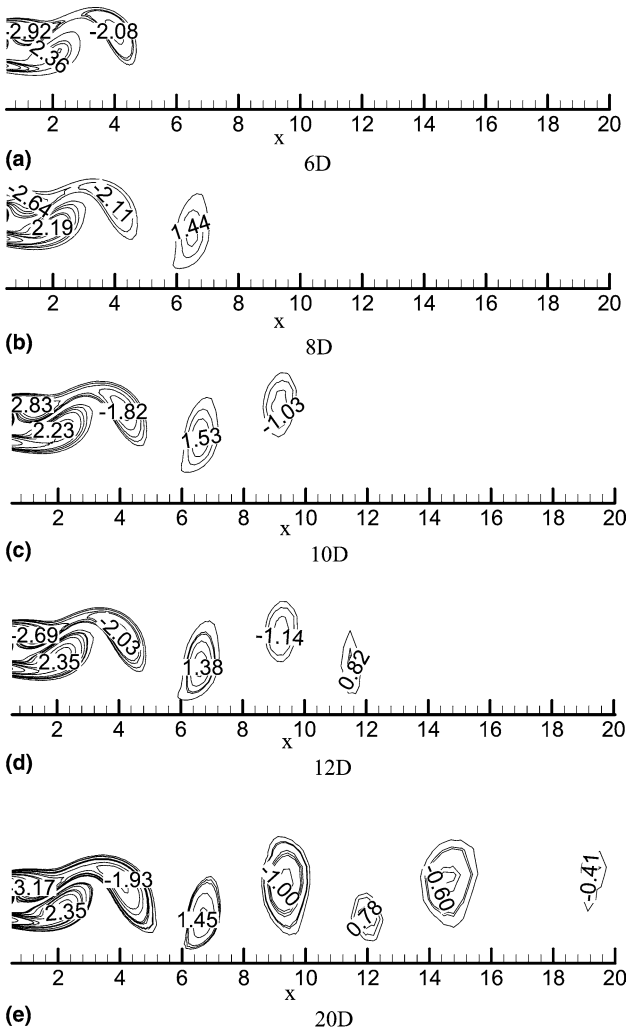

Fig. 10. Instantaneous vorticity contours for circular cylinder near outflow boundary for different boundary placements of (a) 6D (b) 8D (c) 10D (d) 12D (e) 20D at $Re = 100$.

taken at the same phase of the shedding cycle for comparison. It can be seen that there is no distortion of vortices near the exit as the outer boundary is brought closer from 20D to 6D. The contour values indicate that the flow field is only slightly affected by bringing the outer boundary nearer to the cylinder. To observe the effects of boundary placement on the flow pattern, stream function contours at the same phase of the shedding cycle for outer boundary placements at 6D, 8D, 10D, 12D and 20D are shown in Figs. 11(a)–(e). These figures show that the different boundary placements have a negligible effect on the flow structure in the wake and near the cylinder.

5.2. Uniform flow past a square cylinder ($Re = 100$)

Table 3 shows the effect of placement of outer boundary at distances of 6H, 8H, 10H, 12H and 20H from the center of the square cylinder at $Re = 100$. The parameters like St, peak value of C_L and time average

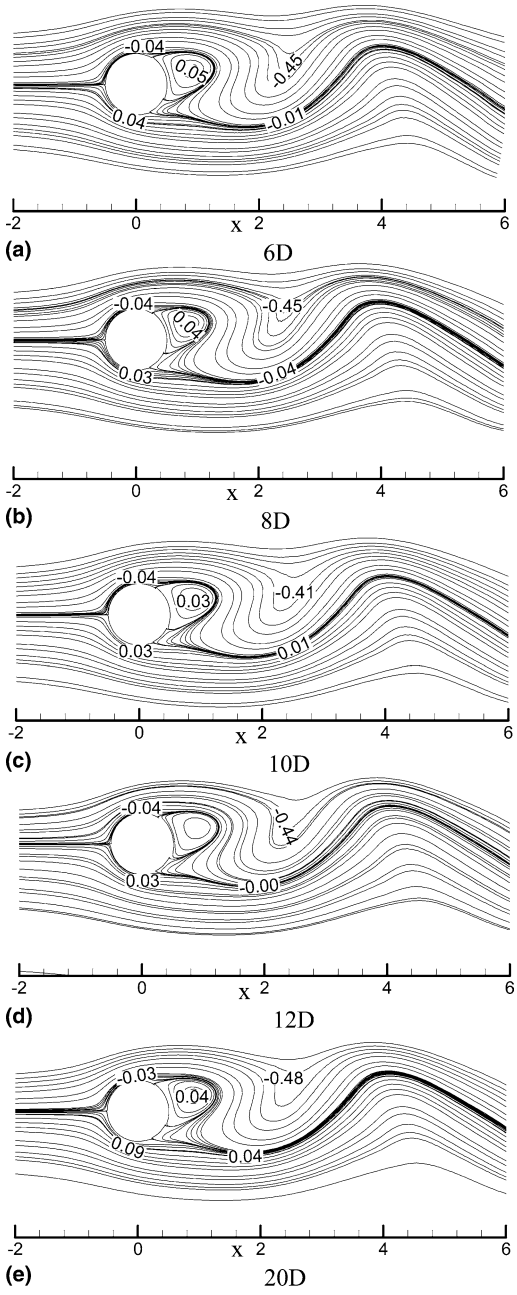

Fig. 11. Instantaneous streamline contours near the circular cylinder for different boundary placements of (a) 6D (b) 8D (c) 10D (d) 12D (e) 20D at $Re = 100$.

drag coefficient $\bar{C}_D$ are compared with the experimental and numerical values given in Refs. [1,8–10], respectively. The values of C_L and $\bar{C}_D$ are rescaled by a factor of 0.5 according to the definitions in [8–10]. In the case of the square cylinder, the numerical data available in [8–10] involve blockage effects due to the use of zero tangential stress conditions on the lateral portions of the outer boundary. No such

Table 3
The effect of far field boundary placement on Strouhal number and peak lift coefficient for uniform flow past the square cylinder at $Re = 100$

Far field boundary	Strouhal number (St)	Peak lift coefficient (C_L)	Average drag coefficient ($\bar{C}_D$)
6H	0.1459	0.1334	1.533
8H	0.1449	0.1345	1.499
10H	0.1438	0.125	1.4708
12H	0.14388	0.125	1.4045
20H	0.14388	0.1255	1.4
Numerical	0.159 [10], 0.147 [9]	0.13 [9]	1.4 [9]
Experimental	0.1410–0.1450 [1]	–	–

conditions have been utilized in the present work and hence the values reported are free from such blockage effects. As discussed in [8,9], blockage effects tend to cause a slight increase in the value of St and the peak value of C_L. Thus, values in Table 3 must be interpreted accordingly in drawing comparison with the numerical data. The value of St and peak value of C_L at 20H are lower than those reported in [8–10] due to blockage effects. Further, the value of St agrees quite well with the experimental data. The primary issue is the change in these values as the boundary is brought closer. The value of St and peak value of C_L increase by 1.4% and 6.3%, respectively, in relation to their corresponding values at 20H, as the outer boundary is brought closer from a distance of 20H to 6H. Here, again it is observed that while there is negligible difference in values of St, the values of C_L are affected more in bringing the outer boundary closer to the cylinder. Increase in C_L, of the order of 5–6%, as in the case of circular cylinder, is observed only for outer boundary placements of 8H and 6H. A similar trend is observed in the values of $\bar{C}_D$ with a 5% increase as the boundary is brought closer from 20H to 6H.

Fig. 12 shows the variation of C_L with time for different boundary placements. From the figure it is clear that there is a phase shift and there is a delay in the inception of instability. These effects are due to the placement of outer boundary.

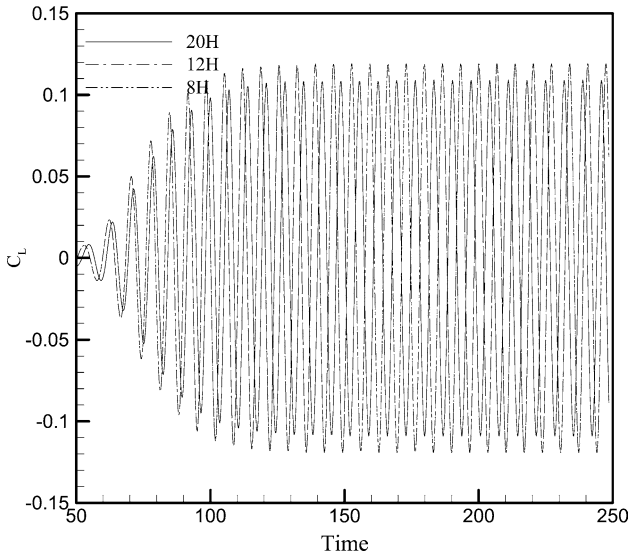

Fig. 12. Variation of C_L at $Re = 100$ for different boundary placements for flow past a square cylinder.

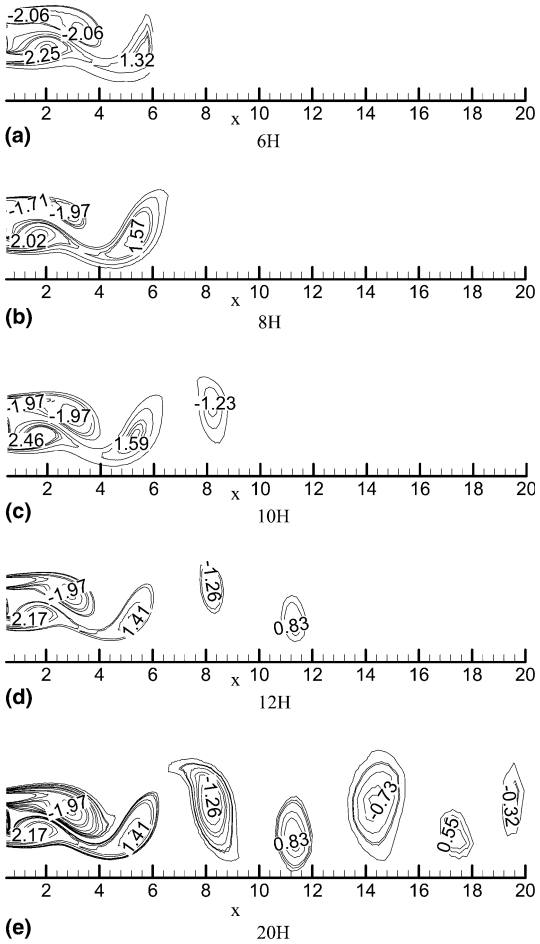

Fig. 13. Instantaneous vorticity contours for square cylinder near outflow boundary for different boundary placements of (a) 6H (b) 8H (c) 10H (d) 12H (e) 20H at $Re = 100$.

Figs. 13(a)–(e) show the instantaneous vorticity contours in the wake and near the exit for different outer boundary placements at the same phase of the shedding cycle. It can be seen from the figures that there is no distortion of vortices as the outer boundary is brought closer to the cylinder from 20H to 6H. Figs. 14(a)–(e) show instantaneous stream line patterns for different outer boundary placements at same phase of the shedding cycle. This trend is similar to the one observed for the case of circular cylinder.

From the above observations, it can be stated that the application of PBC leads to a reasonably accurate prediction of the unsteady flows investigated in this work even for a heavily truncated domain (6–8 times the characteristic size of the body). The usage of PBC does not yield any distortion in the structure of the flowfield near the outflow boundary even for the placement of the outflow boundary at relatively short distances from the body. Most significantly, as the outflow boundary is brought closer, the temporal evolution of the unstable mode or perturbation is least affected as far as its amplitude growth rate and the frequency is concerned. Thus, while PBC is suitable for computing of incompressible flows around immersed bodies, it also appears to have good potential for carrying out a global, linear stability analysis of such flows.

The proposed extrapolation procedure has a stronger physical basis than CBC for incompressible flows around immersed bodies which are governed by parabolic–elliptic equations. The proposed method can be

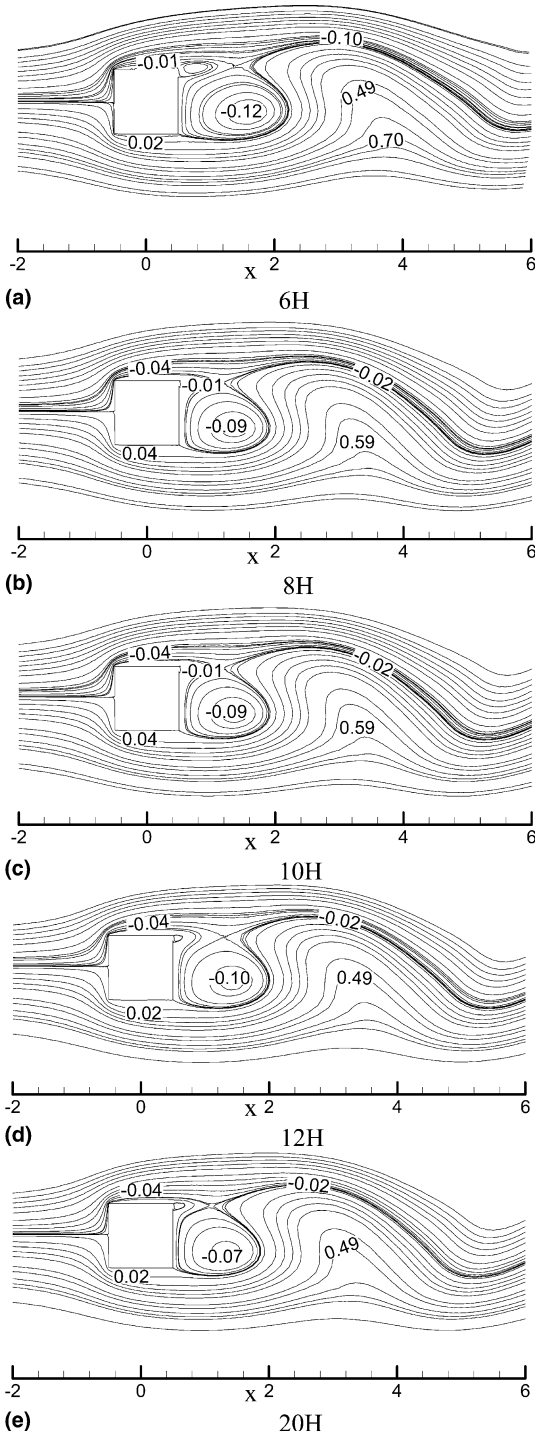

Fig. 14. Instantaneous streamline contours near the square cylinder for different boundary placements of (a) 6H (b) 8H (c) 10H (d) 12H (e) 20H at $Re = 100$.

implemented numerically in a straightforward non-iterative manner on different types of grids adding little to the overall computations.

The main limitation of the method is that for problems involving spatially growing disturbances, the method is not expected to work well on a heavily truncated domain. This is because the assumption of spatially decaying vorticity in determining the variation of circumferential velocity 'v_θ' in the radial direction is in conflict with such a scenario. However, an investigation involving such a situation is actually needed to ascertain the performance of PBC. From the computational viewpoint, the only limitation comes from the fact that the extrapolation from the interior has to be in the radial direction. This involves a slightly greater computational effort on a Cartesian structured as well as on an unstructured grid. However, the character of extra computations involved in such situations is essentially non-iterative and therefore it can be argued that such computations do not contribute significantly to the overall computational effort.

6. Conclusions

In the present work, a new approach for handling outflow boundary condition based on the radial behavior of the velocity field at large distances from the body in external incompressible viscous flows has been presented. While the theoretical basis of this approach has been known for a long time [13], surprisingly it has not been used in numerical computations for such class of flows. It has been demonstrated that the numerical implementation of this methodology is quite straightforward. The validity and the performance of the method has been demonstrated through the classical problems of uniform flow past a circular and a square cylinder.

For these class of problems, it has been demonstrated that usage of PBC leads to accurate predictions even on a heavily truncated domain. Thus, the computational efficiency of such class of flows can be significantly enhanced by employing these boundary conditions. The issue of computational efficiency is even more relevant for 3D computations. The development of boundary conditions in an analogous manner for a 3D scenario and the subsequent assessment of its performance would be a part of future endeavors.

References

[1] A. Okajima, Strouhal numbers of rectangular cylinders, J. Fluid Mech. 123 (1982) 379–398.
[2] N. Stegell, N. Rockliff, Simulation of the effects of body shape on lock-in characteristics in pulsating flow by the discrete vortex method, in: Proceedings of the 3rd International Colloquium on Bluff Body Aerodynamics and Applications, VA, 1996.
[3] I. Orlanski, A simple boundary condition for unbounded hyperbolic flows, J. Comput. Phys. 21 (1976) 251–269.
[4] F.M. Najjar, S.P. Vanka, Simulations of the unsteady separated flow past a normal plate, Int. J. Numer. Meth. Fluids 21 (1995) 525–547.
[5] F.M. Najjar, S. Balachandran, Low frequency unsteadiness in the wake of a normal flat plate, J. Fluid Mech. 370 (1998) 101–147.
[6] L. Cheng, S. Armfield, A simplified marker and cell method for unsteady flows on non-staggered grids, Int. J Numer. Meth. Fluids 21 (1995) 15–34.
[7] L.L. Pauley, P. Moin, W.C. Reynolds, The structure of two-dimensional separation, J. Fluid Mech. 220 (1990) 307–441.
[8] M.P. Arnal, D.J. Goering, J.A.C. Humphrey, Vortex shedding from a bluff body adjacent to a plane sliding wall., J. Fluids Eng., Trans. ASME 113 (1991) 384–398.
[9] A. Sohankar, C. Norberg, L. Davidson, Low-Reynolds-number flow around a square cylinder at incidence: study of blockage, onset of vortex shedding and outlet boundary condition, Int. J. Numer. Meth. Fluids 26 (1998) 39–56.
[10] A.K. Saha, K. Muralidhar, G. Biswas, Transition and Chaos in 2D flow past a square cylinder, J. Eng. Mech. 126 (5) (2000) 523–532.
[11] M. Braza, P. Chassing, H.H. Minh, Numerical study and physical analysis of the pressure and velocity fields in the wake of a circular cylinder, J. Fluid Mech. 165 (1986) 79–130.
[12] C. Hirsch, Numerical Computation of Internal and External Flows, Wiley–Interscience/Wiley, 1990.
[13] K. Karamchetti, Principles of Ideal Fluid Aerodynamics, Wiley, New York, 1966.

[14] Z.U.A. Warsi, J.F. Thompson, C.M. Mastin, Numerical Grid Generation (1984).
[15] C.M. Rhie, W.L. Chow, Numerical study of the turbulent flow past an aerofoil with trailing edge separation, AIAA J. 21 (7) (1983) 1525–1532.
[16] A.A. Amsden, F.H. Harlow, The SMAC method: a numerical technique for calculating incompressible fluid flows, Los Alamos Scientific Report, LA 4370, 1970.
[17] S.W. Kim, T.J. Benson, Comparison of the SMAC, PISO and iterative time advancing schemes for unsteady flows, Comput. Fluids 21 (1992) 435–454.
[18] M. Peric, Efficient semi implicit solving algorithm for nine-diagonal coefficient matrix, Numer. Heat Transfer 11 (1997) 251–279.
[19] P.M. Gresho, Incompressible fluid dynamics: some fundamental formulation issues, Annu. Rev. Fluid Mech. 23 (1991) 413–454.
[20] M. Coutanceau, R. Bouard, Experimental determination of the main features of the viscous flow in the wake of a circular cylinder in uniform translation. Part 1. Steady flow, J. Fluid Mech. 79 (1977) 231–266.
[21] A.S. Grove, F.H. Shair, E.E. Peterson, A. Acrivos, An experimental investigation of the steady separated flow past a circular cylinder, J. Fluid Mech. 19 (1964) 60–80.
[22] D. Barkley, R.D. Henderson, Three dimensional Floquet stability analysis of the wake of a circular cylinder, J. Fluid Mech. 322 (1996) 215–241.
[23] H.M. Blackburn, R.D. Henderson, A study of two dimensional flow past an oscillating cylinder, J. Fluid Mech. 385 (1999) 255–286.